Lanthanum-based dendritic mesoporous nanoplatform for tumor microenvironment activating synergistic anti-glioma efficacy

Guangwei Zheng [a,c,1], Shizhong Wu [a,1], Xianming Deng [a,1], Ao Wang [b], Yunfei Ying [b], Siyaqi Li [b], Feifei Wang [b], Xiaolong Liu [b,c], Peiyuan Wang [b,c,*], De Wei [a,c,**]

[a] Department of Neurosurgery, Shengli Clinical Medical College of Fujian Medical University Fujian Provincial Hospital, Fuzhou University Affiliated Provincial Hospital, Fuzhou, PR China
[b] Fujian Institute of Research on the Structure of Matter, Chinese Academy of Sciences, Fuzhou, 350002, PR China
[c] The United Innovation of Mengchao Hepatobiliary Technology Key Laboratory of Fujian Province, Mengchao Hepatobiliary Hospital of Fujian Medical University, Fuzhou, 350025, PR China

ABSTRACT

Lanthanum (La)-based nanotherapeutics are therapeutically advantageous due to cytoplasmic oxygen species (ROS) levels for mediating intrinsic and extrinsic tumor cell apoptosis. While they have not been extensively explored for their potential to suppress malignancies *in vivo*. Correspondingly, we have formulated a unique lanthanum nanocarrier with high specific surface area, dendritic-divergent mesopores, importantly, exposing more active lanthanum sites. After surface PEGlytion and ICG loading in mesoporous channels, this fantastic nanoplatform can efficaciously enrich in malignant glioblastoma regions. Meaningfully, it can be sensitively dissociated for La ions release under weak acid (pH = 6.5) tumor microenvironment. Upon 808 nm light irradiation, high light-heat conversion efficiency is further proved, then this satisfied thermal in the tumor site progressively enhances ROS production by La ions. Owing to the synergistic oxidative therapy and photothermal therapy of our dendritic La nanoplatform, glioblastoma is efficaciously and synergistically prevented both *in vitro* and *in vivo*. All outcomes highlight the therapeutic potency of La based nanoplatform with radial mesopores to treat malignant cancer *in vivo* and encourage future translational exploration.

1. Introduction

Malignant glioblastoma (GBM), occurs in the central nervous-system, is commonly known as the most aggressive tumors with increasing incidences recently. Surgical resection of GBM is the standard clinical care followed by radiation and chemotherapy, whereas the survival rate of GBM patients has not substantially improved with the limited median survival periods of 10–15 months [1–3]. Furthermore, traditional cancerous therapies of GBM still face huge challenges, like multi-drug resistance, systemic toxicity. In tumor cells, reactive oxygen species (ROS) can maintain dynamic equilibrium balance and are markedly compromise the tumor therapeutic efficiency [4–8]. Typically, extracellular overproduced ROS enrichment is able to fundamentally disturb the oxidative stress homeostasis, eventually inducing apoptosis

or necrosis of tumor cells that is often regarded as oxidative therapy (OXT) [9–11]. Enormous oncological administration modalities are indispensable with ROS over-generation in cytoplasm of tumor tissues. They have been spawned recently, including photo-dynamic therapy, radio-dynamic therapy, chemo-dynamic therapy and micro-dynamic therapy. These treatments have been becoming promising and encouraging therapeutic approaches against malignant tumor [12–17]. Further, the complex and hostile tumor-microenvironment in GBM presents weak acid extracellular, severe hypoxia, relatively elevated concentration of H_2O_2 and GSH in cytoplasm which often boost the proliferation, invasion and metastases of cancerous cells [18–26]. Hence, the combinational administration accompanied with tumor-microenvironment stimuli is critical for eradiating primary GBM. Unfortunately, insufficient exogenous (pH = 6.5) or endogenous (H_2O_2,

GSH and hypoxia) stimuli in tumor tissues as well as some inherent shortcomings of ROS, like short duration of life, diffusion distance limitation, high-reactivity and *in vivo* uncontrollable biological process are capable of hindering clinic application of therapeutic modalities based on ROS, especially the deep GBM treatment [27–30]. Therefore, it is of great significance and an emerging direction that attracts considerable attention to precisely augment ROS production efficacy in tumor tissues.

Lanthanum (La) is commonly known as a rare earth element, studies to this element has previously demonstrated cytotoxic and anti-tumor ability on account of its unique *f*-electropositive configuration. It often includes radio-sensitization *via* the typical Auger effect and more conventional chemotherapeutic synergistic effect *via* amplified apoptotic activity [31–35]. Even though La-based compound has not been completely investigated in GBM setting, but presents two unparalleled advantages that endow it an element of great interest to combat GBM. Firstly, it has been reported that compared to the normal astrocyte cells, GBM cells exhibit a natural tendency to enrich La and its free La^{3+} in cytoplasm [36]. Secondly, La can form stable lanthanum oxide (La_2O_3) that can be engineered into nanocomposites. They can be further applied to circumnavigate the Blood Brain Barrier (BBB) that has been proven a natural hindrance to otherwise prospective nanotherapeutics [37]. To date, very little reports have been investigated La-based nanoparticles for their potential to specially concentrate GBM. Intriguingly, for augmenting the ROS production, phothermal therapy (PTT) induced high local temperature in the tumor site could substantially improve the oxidative stress levels *via* accelerating the ROS productivity [38,39]. Undoubtedly, OXT with synergistic PTT is a meaningful and promising tactic for total ablation of malignant cells. As a clinic approved contrast agent for fluorescent bio-imaging, indocyanine green (ICG) can be also extensively applied to PTT under near-infrared region (NIR) light shining. Encouragingly, its off-peak light in the second window of NIR (NIR II, 1000–1700 nm) is favorable for establishing early, precise, and high-resolution cancer tissue screening [40–42]. Receptor ligand-free mesoporous silica nanocarriers represent a promising avenue for targeted brain tumor therapy, especially for blood brain barrier (BBB) crossing [43,44]. Nevertheless, the currently available tumor microenvironment triggered mesoporous La-based nanoplatform equips with ICG co-delivery for accurate malignancy diagnosis along with incorporating synergistic PTT-OXT of brain tumor is rarely reported.

Building on these investigations, we have engineered a unique dendritic mesoporous lanthanum oxide nanoparticle (MPLa) *via* a universal strategy of viscosity-mediated assembly. Followed by covalent grafting of PEG_{2000} on the surface, afterwards, because of incomparable high specific surface area, ICG dyes are infused into the mesoporous channels (MPLa&ICG), which impart capabilities of fluorescent bio-imaging and photothermal ablation toward GBM (Fig. 1). Under NIR II fluorescent imaging observing, this novel mesoporous nanoplatform can accurately concentrate at GBM tissues after being injected *via* caudal vein of G422 brain tumor bearing nude mice. Importantly, it can be decomposed into La^{3+} ions with ICG discharging under tumor microenvironment with pH = 6.5. Concurrently, beneficial to the high exposure of La ions, high ROS efficiency can be successfully achieved in cytoplasm of tumor cells. Owing to the robust NIR absorption of MPLa&ICG, the induced high thermal preferentially exerts pronounced ROS generation *via* La^{3+}, resulting in boosting the apoptotic/necrotic effect of GBM tumor cell both *in vitro* and *in vivo*. Therefore, this promising mesoporous lanthanide based nanoplatfrom is capable of being designed for accurate delineating and synergistic oncotherapy of clinic gliomas.

2. Experiment

2.1. Preparation of MPLa

Here, MPLa (La3) was synthesized by a conventional assembly strategy *via* viscosity mediation. Briefly, 10 mL of H_2O containing 15.0 mg of $LaCl_3\bullet6H_2O$, 20.0 mg of Hexadecyltrimethylammonium bromide
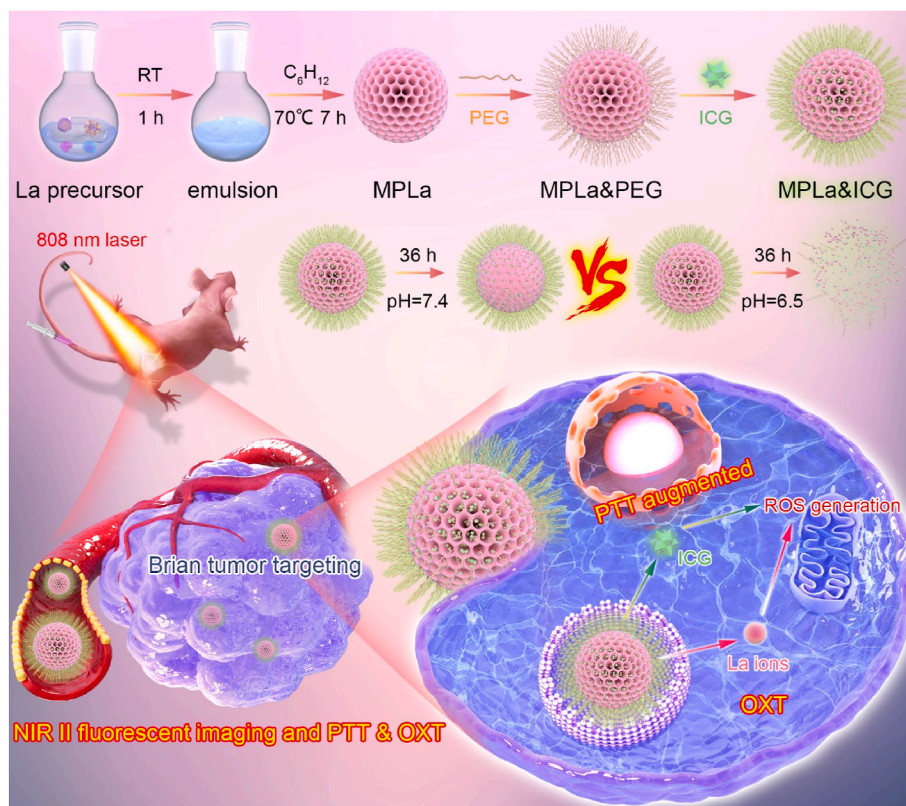
Fig. 1. Schematic procedure to construct a La based nanosphere with ICG loading in dendritic mesopores and surface PEGylating for NIR II bioluminescence imaging and synergistic treatment of PTT& OXT.

(CTAB), 3.0 mg of hexamethyleneimine (urotropin), 12.0 mg of sodium salicylate and 2.0 mg of citric acid were first mixed together and ultrasonicated for about 10 min. Then the mixture was kept with vigorous stirring after 5.0 ml of cyclone hexane was introduced at room temperature. Subsequently, above reaction system was move to a 70 °C oil bath and maintained stirring for 7 h. Finally, MPLa product was isolated by a centrifugation (10000 rpm, 15 min) and washed 3 times with ethanol for removing the residual urotropine. Further, in order to realize CTAB surfactant removal, re-dispersed the obtained MPLa in 100 mL of acetone and refluxed at 60 °C for 12 h. After washing by H_2O, the final product was dried at vacuum (60 °C, 12 h). La1, La2 and L4 with different doses of $LaCl_3 \bullet 6H_2O$ and volume ratios of water/cyclone was prepared as the same procedure.

2.2. Preparation of MPLa&PEG

For extending blood retention and avoiding immunogenicity, the surface of this mesoporous nanoparticle was conducted PEG_{2000} coating. In brief, 25 mg of PEG_{2000}, 100 mg of MPLa and 10 mL of H_2O were mixed together and magnetically stirred at 37 °C for more than12 h. Then the PEG modified MPLa precipitate was separated by centrifugation (10000 rpm, 15 min). For eliminating the residual PEG_{2000}, the dendritic mesoporous product, MPLa&PEG was washed by ethanol for 3 times (10000 rpm, 15 min). Then the sample was dried by a vacuum overnight and refrigerated for the following preparation.

2.3. Preparation of MPLa&ICG

The final MPLa&ICG was engineered as follows. A total 5 mL, 1 mg/mL of MPLa&PEG aqueous solution (dispersed in H_2O) was added to a solution containing 5 mL, 200 µg/mL of ICG (dispersed in H_2O). Latterly, after 30 min of ultrasonic treatment for mono-dispersion, the mixed reaction system was continuously oscillated for 3 h (25 °C, 180 rpm). Lastly, the mesoporous precipitate was separated by a high-speed centrifugation (10000 rpm, 15 min), the sample of MPLa&ICG was successfully prepared after 3 times washing by H_2O to remove the unabsorbed ICG. Re-dispersed the nanoplatform in 10 mL of H_2O.

2.4. Endocytosis evaluation of MPLa&ICG

The cellular uptake of MPLa&ICG was investigated and imaged by a confocal laser scanning microscopy (CLSM). Briefly, G422 glioma cells were firstly seeded into 6-well plates at a concentration of 1×10^5 per well with 1 mL of DMEM fresh medium (10 % FBS, 100 units/mL of penicillin, 100 µg/mL of streptomycin) for 24 h of incubation. After the separate treatment with free MPLa&ICG, hollowed virus inspired La oxide nanocarriers with comparative ICG loading ($HvLaO_2$&ICG) and the same concentration of ICG (5 µg/mL), the G422 brain cancer cells were incubated for 12 h. Then, all the cell samples were washed by PBS 1X for 3 times and 1 µg/mL DAPI was subsequently applied for staining cellular nuclei for 30 min and cellular fluorescent imaging of the uptake nanoformulations (Ex 660 nm, Em 700–750 nm) was conducted by a confocal laser scanning microscope (CLSM).

2.5. Intracellular ROS estimation

G422 brain tumor cells were firstly harvested and seeded in a 6-well plate. After 12 h of co-culture at a 37 °C incubator, the cells were washed by PBS and treated with MPLa&ICG (dispersed in fresh cell medium). After immersion for 12 h, cells from above three groups were irradiated by an 808 nm laser (P = 1.5 W/cm², t = 5 min) followed by another 2 h incubation. Then the cellular medium was discarded and the breast cancer cells were rinsed by PBS. Subsequently, 1 µM of 2′,7′-dichlorodihydrofluorescein diacetate (DCFH-DA: Ex 488 nm, Em 500–550 nm) dispersed in fresh medium was utilized to stain the intracellular ROS. After 30 min incubation, the cells were rinsed 3 times by PBS. The cell

samples were then fixed and the nuclei was stained by DAPI (Ex 360 nm, Em 400–450 nm). Finally, all samples were imaged by a CLSM. Control G422 cells were directly administrated with PBS, MPLa&ICG, $HvLaO_2$&ICG nanoparticles and fluorescent cellular bioimaging was conducted by same procedure.

2.6. Preparation of animal models

All animal studies were conducted under a protocol approved by the Institutional Animal Care and Use Committee of Fujian Medical University (IACUC-FPH-SL-20231020[0183]). Female BALB/c nude mice were bought from GemPharmatech Co., Ltd (Nanjing, China). Subcutaneous murine brain tumor bearing nude mice were established by subcutaneously inoculated 0.1 mL of G422 cells (2×10^6 cells per mouse, saline dispersion) on the right hind-leg of BALB/c mice (6-week-old, 18–20 g). Subsequent fluorescent imaging and tumor eradication studies were carried out when the tumor volume grew to 100–200 mm³ after post injection of tumor cells for two weeks.

2.7. In vivo tumor enrichment

MPLa&ICG, ICG was separately administrated into the tail-vein of subcutaneous tumor bearing mice. After various post injection hours, the injected mice were immediately observed by a homemade NIR II luminance bio-imaging equipment (808 nm NIR laser irradiation, 100 mW/cm²) with 1000 nm longpass filter installing. Besides, mice from above two groups were scarified at 24 h post injection, vital organs including whole tumor, heart, liver, spleen, lung and kidney were isolated and further imaged by ex vivo NIR II illuminant bioimaging. Meanwhile, the quantitative fluorescence intensities from all tissues were determined to calculate the corresponding bio-distribution.

2.8. Photothermal generation in tumor

For assess the photothermal generation in vivo, MPLa&ICG, PBS (control) was separately injected into the tail-vein of subcutaneous GBM tumor bearing mice. Tumor sites were continuously illuminated by an 808 nm light (P = 1.5 W/cm², t = 6 min) at 24 h post injection. The thermal bio-pictures were immediately photographed by an infrared thermal camera.

2.9. In vivo anti-GBM evaluation

Firstly, GBM-bearing nude mice were stochastically divided into 4 groups (tumor volume ~100 mm³, n = 4). Then mice were separately injected with various formulations (10 mg/kg) (PBS, PBS + L, MPLa&ICG, and MPLa&ICG + L) for once via vena-caudalis. Mice from the laser treated groups were continuously illuminated by an 808 nm light (P = 1.5 W/cm², t = 6 min) at 24 h post injection. Then, to study the anti-tumor capability of single OXT and synergistic OXT&PTT, the body weight and tumor size (including length & width) were accurately detected every 3 days. During the whole treated period (15 days), the tumor volume values from all groups were calculated 5 times according to the formula as follows: Tumor volume = length × width × width × 0.52. On day 15, mice from all group were euthanized, tumor tissues were separated, weighted, separately stained with hematoxylin & eosin (H&E) and terminal deoxynucleotidyl transferase dUTP nick end labeling (TUNEL). Concurrently, all vital organs (including Heart, Liver, Spleen, Lung, Kidney) were carefully exfoliated for the final H&E staining.

3. Results and discussion

3.1. Fabrication of MPLa nanospheres

In this study, typically, the MPLa nanospheres can be successfully

constructed in a water-oil bi-phased system *via* a viscosity mediated nano-assembly method. The exact steps for MPLa nanospheres are illustrated in Fig. S1. In a mixed solution, cyclohexane plays the part of oil-phase which is introduced to an aqueous water system. It includes methenamine for serving as a redundant, CTAB for acting as a structural directing agent, sodium salicylate for using as the viscosity regulator, citric acid as a cheating-agent and lanthanum chlorides for applying as the lanthanide precursor. Here, the aqueous-phase is proactively stirred homogenous at room temperature, then the oil-phased cyclohexane is immediately poured to above mixed water soluble system. In this

reacted system, citric acid is capable of regulating the hydrolysis efficiency of lanthanum precursor and the interactive force between the hydrolyzed oligomers and the surfactant CTAB micelles. The final MPLa nanospheres are successfully prepared after magnetically stirred for 7 h with temperature maintaining at 70 °C. The obtained series of samples are observed by the transmission electron microscopy (TEM), the size and dispersion of MPLa nanospheres present uniformly. As shown in Fig. 2A–D, when adjust the volume ratio of cyclohexane/water from 0 to 3.0 (La1, 0; La2, 1; La3, 2; La4, 3) and reduce the dose of $LaCl_3 \bullet 6H_2O$ from 1.5 to 0.3 mg/mL (La1, 0.5 mg/mL; La2, 0.75 mg/mL; La3, 1.0 mg/
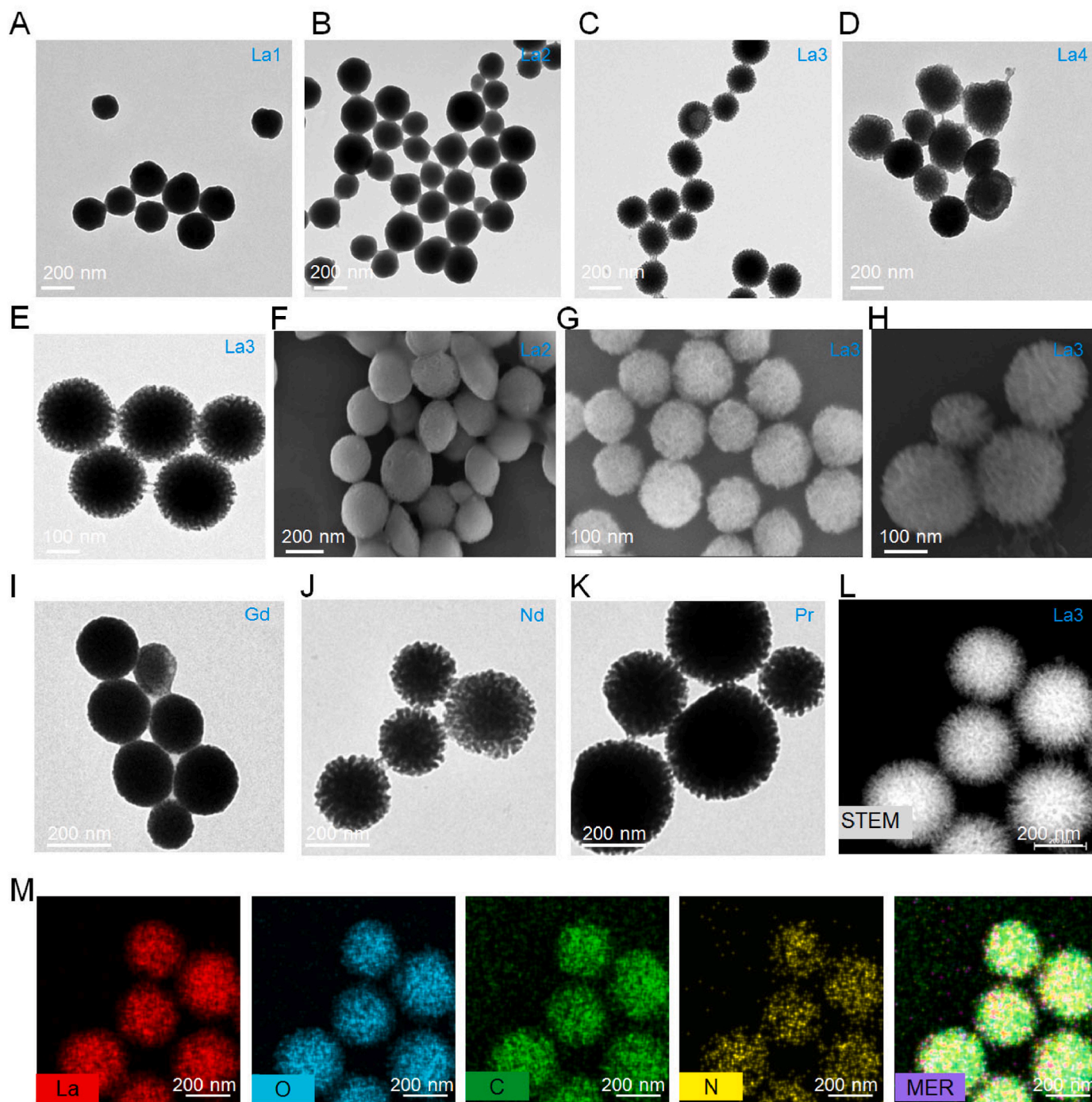
Fig. 2. TEM photographs of MPLa nanospheres with various mesoporous diameters by regulating the volume ratio (water to cyclohexane) (A, La1, 0; B, La2, 1; La3, 2; D, La4, 3) and concentration of $LaCl_3 \bullet 6H_2O$ (A, La1, 0.5 mg/mL; B, La2, 0.75 mg/mL; C, La3, 1.0 mg/mL; D, La4, 1.5 mg/mL). (E) HRTEM image of La3. (F,G) SEM images of La2 and La3. (H) magnified SEM images of La3.TEM photographs of Gd (I), Nd (J) and Pr (K) based dendritic mesoporous nanospheres which was fabricated by the same method as La3. (L) HR-STEM (M) and elemental-mapping images of MPLa (La3).

mL; La4, 1.5 mg/mL) the mesopore diameter is able to tune from 0 nm to 15 nm ~ 200 nm of MPLa (Fig. S2) with pore diameter as ~ 10 nm (La3) is employed in the subsequent *in vitro* characterization and bio-applications. Scanning electron microscopy (SEM) picture also display the size variation of La2 and La3 (Fig. 2F and G), further demonstrating that the pore sizes of lanthanide based nanoparticles can be precisely regulated *via* our strategy. TEM with high-resolution (HRTEM) and magnified SEM images reveal that our homogenous dendritic La based nanospheres possess radial mesoporous channels (Fig. 2E–H). Further, by the same ratio and concentration of precursor as La3, other three kinds of rare-earth (Gd, Nd, Pr) based nanosperes can be successfully fabricated with comparable size and uniform spherical morphology (Fig. 2I–K), evidencing our reliable and versatile strategy to achieve dendritic lanthanide based nanoplatforms. As the atomic weight increases, the molar mass decreases, and the mesopore size correspondingly increases. We have also synthesized other kinds of transition elements, including of Fe, Cu, Mn, while irregular morphologies are visualized (Fig. S3), thus we will further improve this method in the future. Besides, the accurate constitute elements of MPLa are thoroughly studied by an energy dispersive spectrum (EDS) and STEM high-resolution (HR-STEM) (Fig. 2L). The corresponded constitute element mapping images manifest that La, O, C, N is uniformly scattered in every MPLa nanosphere (Fig. 2M). In the end, according to X-ray diffraction (XRD) spectrum, MPLa displays no characteristic peak, revealing an amorphous nanocomposite (Fig. S4). On account of the viscosity mediated assembly method is conducted at room temperature and base on the previous work, the component of the as-prepared MPLa is lanthanum hydroxide.
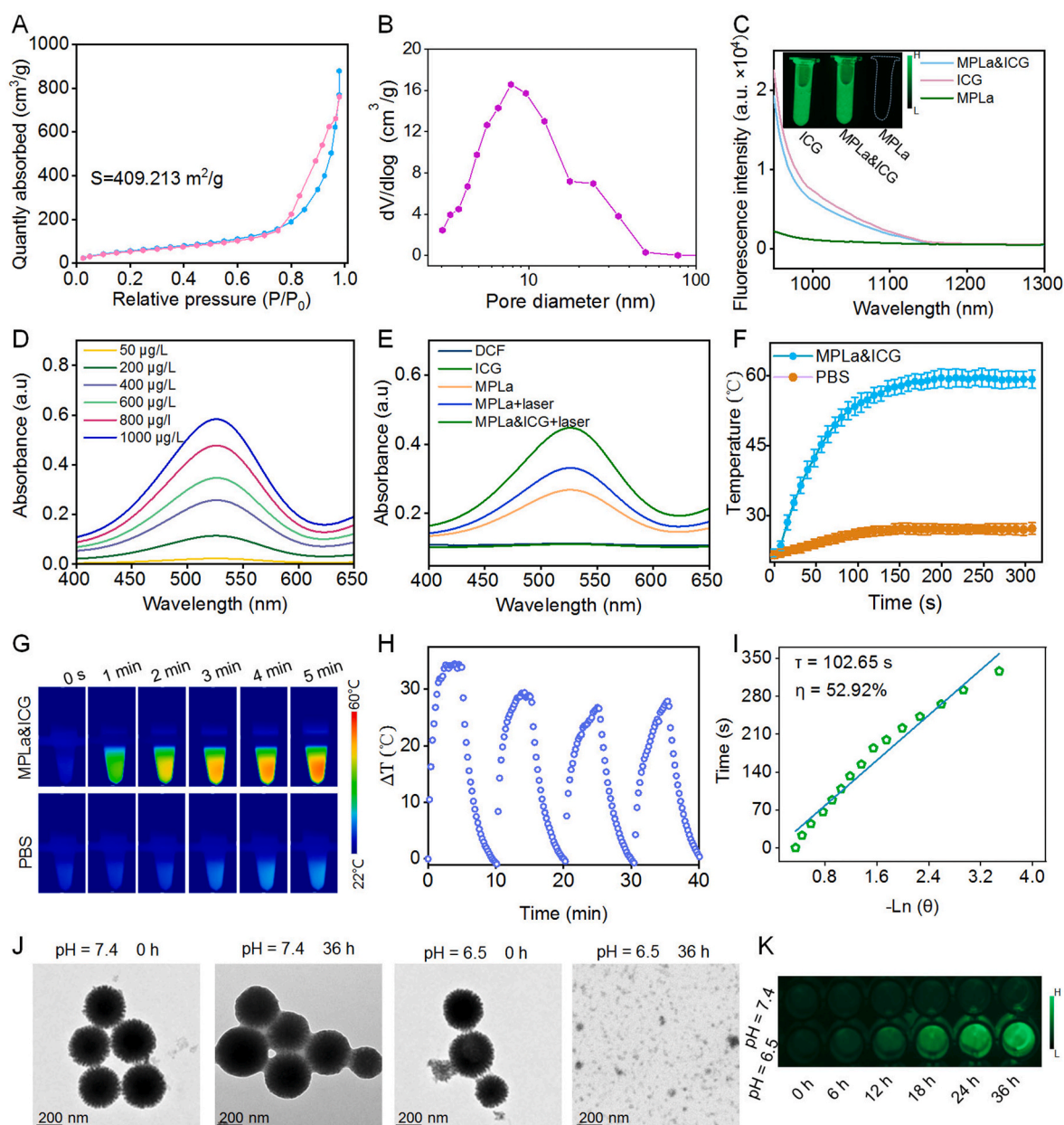
Fig. 3. (A) Specific surface area and (B) pore diameter distribution of MPLa. (C) Emission spectra of ICG, MPLa and MPLa&ICG. Insert, a NIR II fluoresce picture of above samples. (D) ROS generation efficiency of MPLa&ICG + laser at various doses. (E) The variation trend of the fluorescence from DCF after mixed with ICG, MPLa, MPLa + laser and MPLa&ICG + laser. (F) The heating generation curves and (G) thermal images of MPLa&ICG (200 μg/mL), PBS under laser irradiation. (H) Temperature discrepancy of MPLa&ICG over 4 heating/cooling cycles. (I) Linear co-relation of -Ln(θ) and cooling time. (J) TEM photographs of MPLa&ICG dispersed in pH = 7.4, pH = 6.5 stimulated fluid for 36 h. (K) A NIR II florescent picture of MPLa&ICG dispersed in pH = 7.4, pH = 6.5 stimulated fluid for various hours.

3.2. NIR II fluorescent imaging and synergistic effect of ROS generation and PTT in vitro

After successfully synthesized MPLa, we are encouraged to characterize this novel mesoporous lanthanide nanoparticle. The N_2 sorption-isotherms of MPLa that has been constructed *via* the viscosity-mediated assembly approach typically presents type IV curvatures and the surface area is meticulously calculated by the Brunauer-Emmett-Teller (BET) equation. As illustrated in Fig. 3A, it is approximately $\sim$409.213 m^2/g (Fig. 2B). Besides, the average diameter of mesopores is detected as $\sim$11.3 nm, exhilaratingly, it is consistent with both TEM & SEM photographs. Mesoporous reservoir exhibits a relatively high specific surface area and large radial pore-diameter those are instrumental in adsorption/deposition of guest cargos, like therapeutic drugs, DNA and functional protein. Before the mesoporous encapsulation, the La-based surface PEGylation (MPLa&PEG) is formulated for increasing the blood stability and blood retention, thereby allowing an attenuated dosing frequency. Subsequently, in this study, ICG as the fluorescent/therapeutic agent is simultaneously entrapped in the mesopores of MPLa *via* hydrogen-bonding interaction and the π-π stacked conjugation (MPLa&ICG). A standard curve is plotted based on the maximum absorption value of ICG (780 nm), the loading content and loading efficiency of ICG in MPLa&PEG are determined as $\sim$ 29.26 %, 52.43 %, respectively (Fig. S5). Further, the final product is analyzed by a fluorescence spectrometer, as illustrated in Fig. 3C, the off-peak emission spectra of ICG and MPLa&ICG are very consistent. And this beyond 1000 nm (1000 longpass filter) bioimaging of both ICG and MPLa&ICG are also visualized by an imager equipped with an InGaAs detector. Evidently, the luminescence from MPLa&ICG perfectly falls within NIR II, confirming that it can be employed as an appreciable contrast agent in NIR II (Fig. 3C). Then we are inspired to detect the generated ROS efficiency by using DCF-DA which is commonly performed by a simply measurement of the generated product DCF with fluorescence at 525 nm. As shown in Fig. 3D, a unique MPLa&ICG dose-response curves are detected accompanying by an 808 nm laser shining. Additionally, ICG and DCF fail to produce ROS, and thus no light emission could be quantified (Fig. 3E). Fortunately, the most significant emission of DCF is detected in the MPLa&ICG with exposure of 808 nm NIR laser, reaffirming the effect of NIR illumination for the ROS mediating in MPLa. Next, the photothermal performance of MPLa&ICG dispersed in PBS solution are monitored. As depicted in Fig. S6, the temperature variations of MPLa&ICG exhibit a concentration depended profile. The photothermal properties of MPLa&ICG and ICG are also studied by varying the illumination time of NIR laser. The temperature remarkably increases from 26.1 °C and a highest temperature over 60 °C is determined within 5 min. By contrast, in PBS group, slightly temperature increase (28.3 °C) is recorded even at the end time of the thermal study. Thermal photographs of these two groups in Fig. 3G directly confirm the distinct discrepancy in photothermal generation. These outcomes clearly demonstrate the outstanding photothermal conversion performance of MPLa&ICG. Thus, we are delighted to assess the definite light-to-heat conversion efficiency (η), the corresponded thermal stability of MPLa&ICG is studied by multiple on/off NIR laser shining cycles (Fig. 3H). Owing to the quenching of water molecules toward surface anchored ICG, the generated thermal presents a distinct decline process in the first cycle, surprisingly, it maintains the heating efficiency after the followed three cycles. The result might be attributed to firmly fixed ICG within the mesoporous channels that further enhances the photostability. Concurrently, accurate η value is determined as $\sim$52.92 % based on a previously fundamental formula calculation (Fig. 3I), which is prominently surpassed the reported lanthanide nanocarries with stacking mesopores for ICG loading [45]. Finally, the degradable feature of MPLa&ICG is evaluated under immersion of weak acid tumor microenvironment fluid (pH = 6.5) and normal biological buffer (pH = 7.4), respectively. The total morphological dissociation with smaller fragments is visualized by TEM after treated with pH = 6.5 buffer for 36 h, on the contrary,

comparable spherical morphology maintains in pH = 7.4 group (Fig. 3J). Significantly, Fig. 3K demonstrates that NIR II fluorescent signal of the discharged ICG from pH = 6.5 group significantly augments over time and reaches the peak value at 36 h. In contrast, undetectable released ICG is monitored under normal condition. Simultaneously, an extremely strong ICG absorption value (780 nm) is observed in the supernatant from MPLa&ICG under pH = 6.5 buffer immersion for 36 h (Fig. S7). Considerably higher La ions is measured in the supernatant from pH = 6.5 treated group at every time points (Fig. S8). Collectively, such obvious differences strongly confirms that our tumor microenvironment condition-triggered MPLa&ICG is able to be explored as a synergistic NIR laser driven photothermal-ROS oxidative nanomedicine.

3.3. Endocytosis, ROS generation and synergistic cell killing

Before performing *in vitro* synergistic therapy, the cellular uptake of MPLa&ICG is observed. Confocal imaging is performed to observe GBM cell (G422) incubated with ICG and MPLa&ICG, respectively. Especially, according to previous reported strategy [46], we have also constructed another La based nanocarriers with staked mesopores for further comparative studies. HvLaO$_2$&ICG, staked mesoporous lanthanum oxide nanocarriers with comparative ICG loading ratio, was successfully fabricated (Fig. S9). Negligible zeta potential variation is determined after PEG molecules anchoring, further both MPLa&ICG and HvLaO$_2$&ICG present similar positive charges, excluding the influence of surface charge on cellular endocytosis (Fig. S10). Apparently, stronger red signal in cytoplasm deriving from HvLaO$_2$&ICG is capable of being visualized in sharp contrast with that from MPLa&ICG (Fig. 4A–C). This outcome is strongly consistent with our reported study that rough nanostructure is beneficial to cytomembrane adhesion. Owing to the relative weight variation of La ions in above two La-based nanoparticles, we are inspired to investigate the discrepancy of endocellular ROS levels *via* an indicator of DCFH-DA. Faint green fluorescent signal is verified in HvLaO$_2$&ICG treated G422 cells, particularly, relatively stronger intensity is discovered MPLa&ICG group. As HvLaO$_2$ contains the main template of virus-like mesoporous silica, above extraordinarily more ROS generation from pure lanthanum nanosphere should be ascribed to more exposed active sites of La ions. Importantly, compared to single MPLa&ICG treated cells, the maximum amount of ROS production is observed in G422 cells with administration of MPLa&ICG plus exposing of NIR laser (Fig. 4B–D). Taking together, even though MPLa shows a relatively lower endocytosis efficiency in comparison with HvLaO$_2$, contrarily, after ICG dye encapsulation, then the fantastic nanoplatform acts as an ideal OXT nanoagent after laser exposure. To obtain deep insight of the synergistic effect for the inhibition of tumor cells proliferation, cell viabilities are meticulously studied. As the concentration of MPLa&ICG increases, slight increased toxicity to G422 cell in dark is determined, manifesting the partial anti-cancer cell effect of single OXT. Noteworthy, cell viabilities in MPLa&ICG + L pronouncedly decrease along with concentrations increasing. Especially, when the dose is set as 300 μg/mL, in comparison with MPLa&ICG group, more than 3-fold higher G422 cells are eliminated in MPLa&ICG + L group, preliminarily testifying the satisfied photo-induced multi-mode therapy (Fig. 4E). In view of above overwhelming cell lethality, intuitively, double-staining (Calcein AM-FITC) protocol is utilized to discriminate live (green light) and dying (red light) G422 cells. As depicted in Fig. 4F and G, indiscoverable dead tumor cells are observed in both PBS (95.33 %) and PBS + L (91.0 %) groups, verifying that the 808 nm laser has no detrimental effect toward cells. While there are partial lethal cells in MPLa&ICG group (72.67 %), indicating that OXT has insufficient ability for tumor cell killing. Interestingly, most of G422 cells emit red light in MPLa&ICG plus laser shining (15.26 %), which demonstrate the complete cellular killing. Additionally, the induced apoptosis/necrosis G422 cells is also estimated by a flow-cytometry. Notably, apoptotic/necrotic G422 cells *via* MPLa&ICG + L mediating is exceptional 3.0 times that of MPLa&ICG administrated cells (Fig. 4H and I). These outcomes
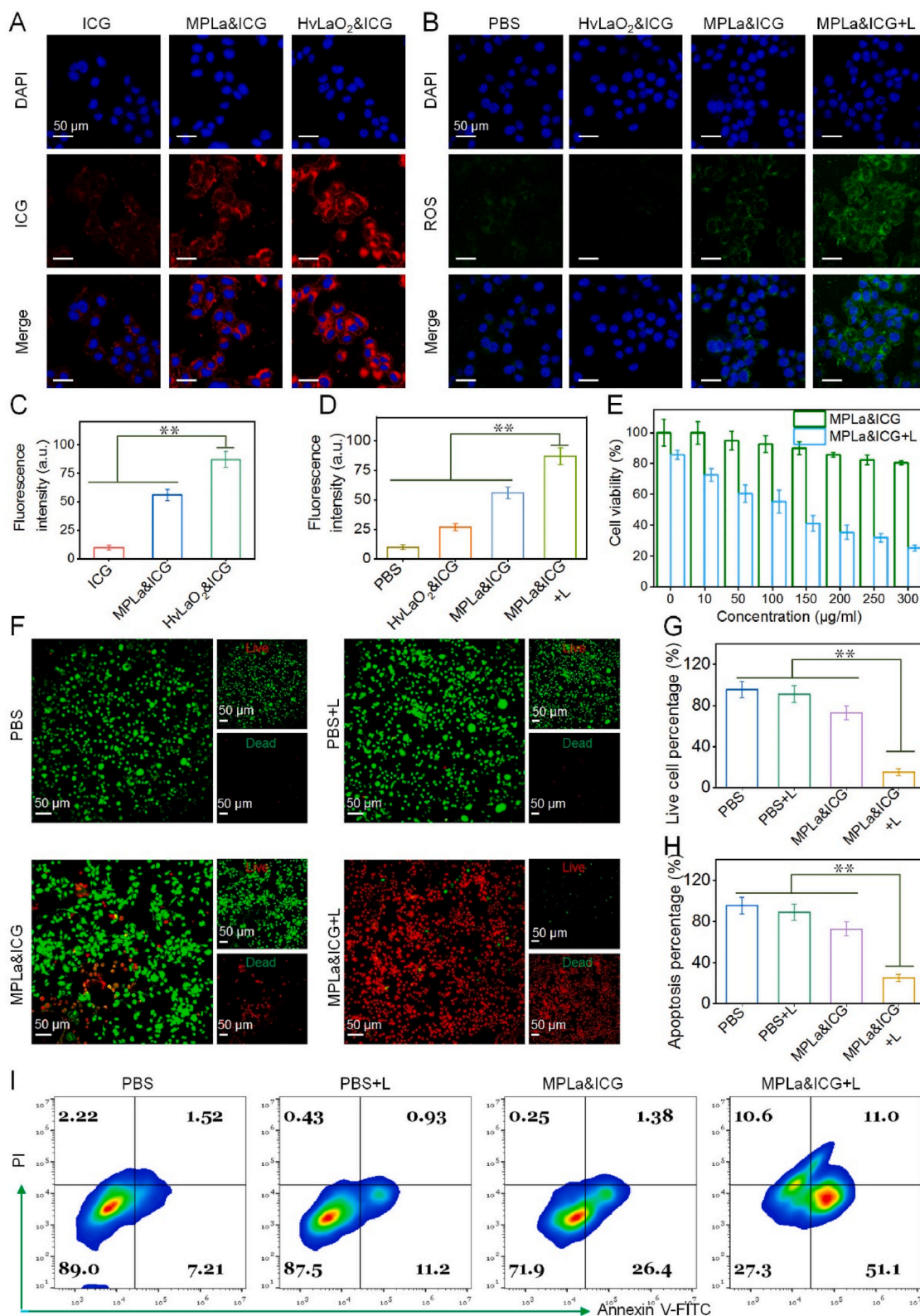
Fig. 4. (A) CLSM pictures and (C) quantitative red fluorescent intensity of G422 cells after cultivated with ICG, MPLa&ICG and HvLaO$_2$, respectively. (B) CLSM images (D) and quantitative green fluorescent intensities of intracellular ROS estimation after administrated with PBS, HvLaO$_2$&ICG, MPLa&ICG and MPLa&ICG + L, respectively. (E) G422 cell viabilities after two day's treatments of MPLa&ICG and MPLa&ICG + L, respectively. (F) Fluorescent pictures of live/dead G422 cells and (G) corresponded quantitative percentages of live cells (stained green) after treated with PBS, PBS + L, MPLa&ICG and MPLa&ICG + L. (H) Apoptotic/necrotic percentages and (I) Apoptotic/necrotic grouping studies of G422 cells after administrated PBS, PBS + L, MPLa&ICG and MPLa&ICG + L. **p < 0.01, data is showed as means ± SD (n = 4).

substantially reflect our La based nanoplatform along with NIR laser illumination is capable of synergistically inhibiting the proliferation of GBM cell, making MPLa&ICG as an extraordinary PTT-OXT nanoagent for clinical GBM ablating.

3.4. *In vivo tumor accumulation and PTT evaluation*

Based on the efficacious *in vitro* cell killing *via* PTT-OXT, initially, tumor accumulation investigation is performed in G422 murine solid tumor-bearing Balb/c nude mice. Before *in vivo* studies, we have assessed the hemolysis of MPLa&ICG. Interestingly, as the concentration increased to 500 µg/mL, any hemolysis phenomenon is measured
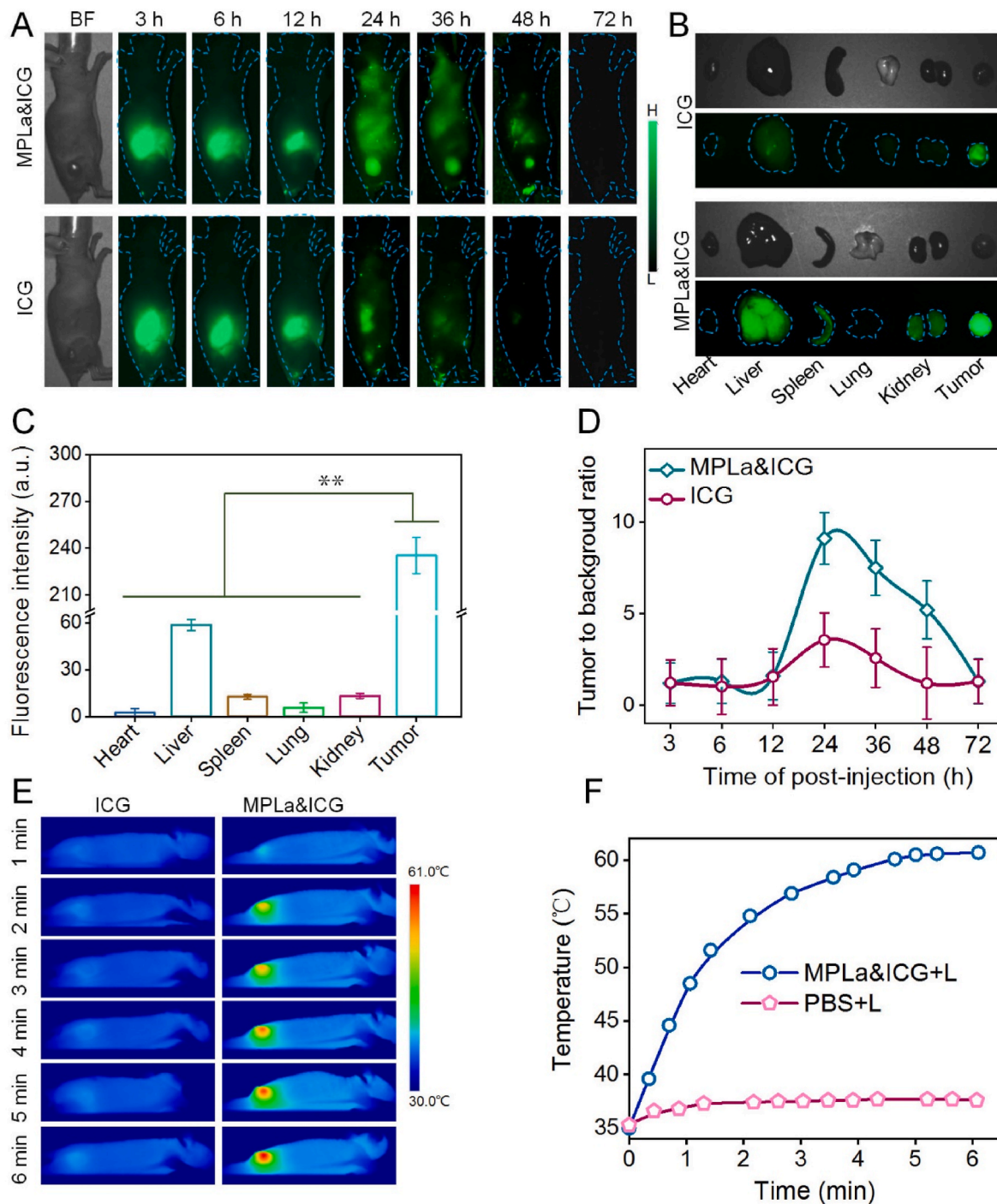

Fig. 5. (A) NIR II fluorescent bi-pictures of G422 marine GBM-bearing nude mice after separately tail-vein injected MPLa&ICG and ICG for various hours. (B) *Ex vivo* fluorescent bio-pictures of vital normal organs as well as tumors dissected from GBM-bearing mice after tail-vein treating of MPLa&ICG and ICG at 24 h post administration, respectively. (C) Tumor to background ratios from NIR II luminescent bio-pictures of various administrations. **p < 0.01, data is showed as means ± SD (n = 4). (D) The quantitative mean NIR II signal intensities from tumor and vital organ tissues after 24 h post tail-vein injection of MPLa&ICG. (E) Infrared-thermographic pictures of GBM-bearing nude mice after separately tail-vein injected PBS, MPLa&ICG for 24 h when continuous irradiation was carried out by an 808 nm laser for different minutes. (F) The corresponded tumor temperature increased profiles over 808 nm laser irradiated time from PBS or MPLa&ICG treated mice.

(Fig. S11), which profoundly proved the good biocompatibility of our nanoplatform *in vivo*. After intravenous injection of MPLa&ICG or ICG *via* caudal-vein, we have monitored dynamic fluorescent changes using a NIR II luminescent imager (808 nm laser shining and 1000 nm longpass filtering) in real-time. The fluorescent signal substantially distributes in liver tissues after 3 h–12 h of tail-vein injections of above two groups. In ICG administrated group, no obvious fluorescent intensity in the tumor tissue is detected during the whole monitoring process (Fig. 5A). Surprisingly, maximum MPLa&ICG concentrate in tumor site with the

tumor boundary being clearly delineated at 24 h post-injection. As the injection time extended, gradually decreased light from tumor site can be clearly observed and there is still NIR II signal residue at the tumor tissues even after tail-vein injection for 2 days (Fig. 5A). According to the *ex vivo* NIR II fluorescence bio-images of vital organ that dissected at 24 h post administration, a tumor from MPLa&ICG treated mouse is significantly lightened up and the corresponded signal intensity is prominently higher than those of reticuloendothelial organs (Fig. 5B and C). Further, quantitative tumor to background (normal tissue in tumor
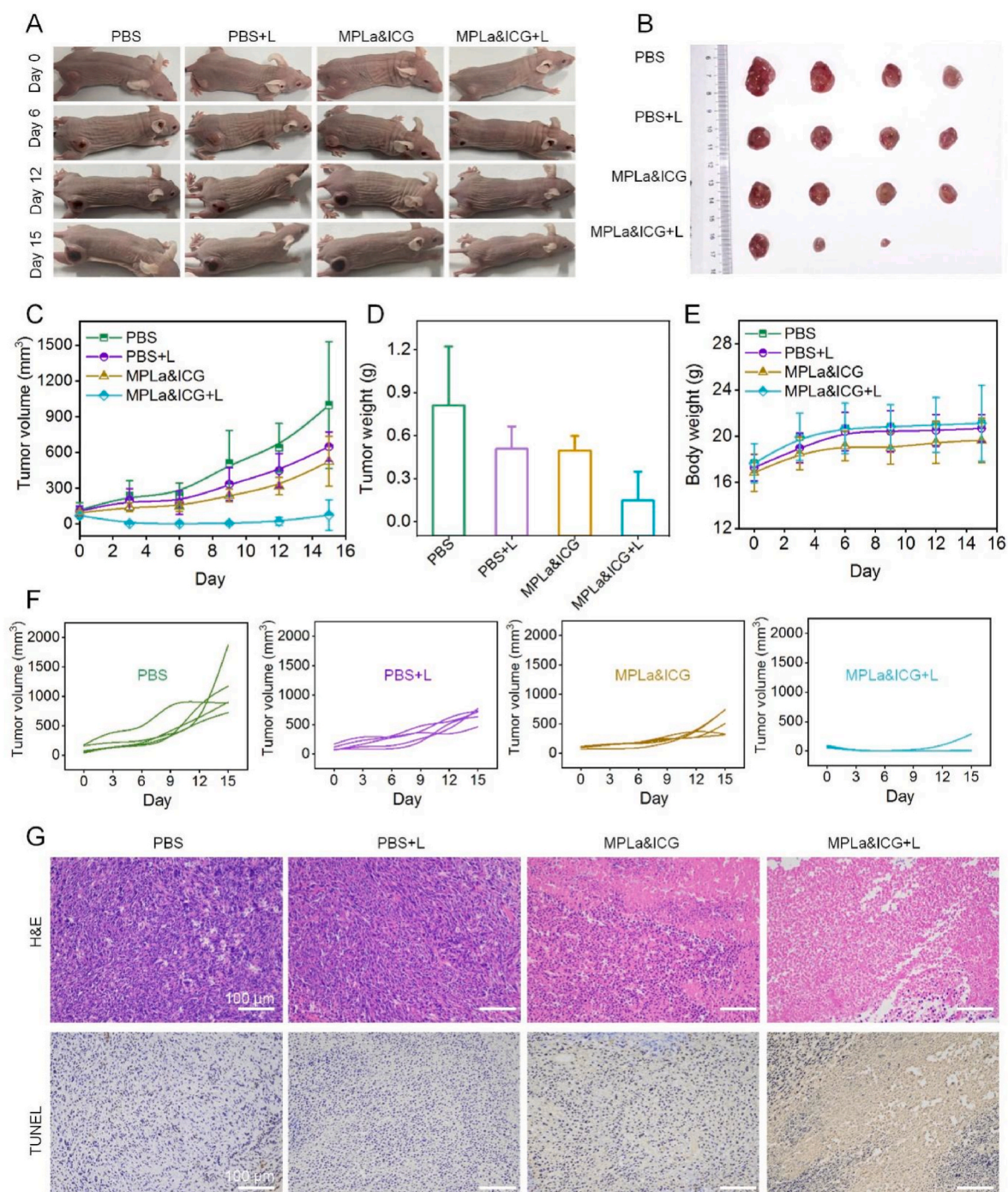
Fig. 6. (A) Representative pictures of GBM bearing mice and (B) the whole resected tumors from all tested groups at day 15. (C) Tumor growth curves of GBM bearing mice after treated with PBS, PBS + L, MPLa&ICG and MPLa&ICG + L for 15 days. (C) The mass of resected GBM tumors from all tested groups at day 15. (F) Individual tumor growth profile after separately administrated with PBS, PBS + L, MPLa&ICG and MPLa&ICG + L for 15 days. (H) H&E and TUNEL stained pictures of the tumor slices after four separate administrations at day 15. (D) Body weight changes after four administrations for 15 days. **p < 0.01, data is showed as means ± SD (n = 4).

periphery) ratio showcases that MPLa&ICG yields relatively higher value than that of ICG. The maximum contrast is discovered at 24 h post injection of MPLa&ICG which is twice as that of ICG group at the same period (Fig. 5C). In short, our ICG loaded mesoprous nanoplatform clearly delineates tumor tissue as a bright-spot against a dark-background of normal tissue at 24 h post administration. Beneficial to the satisfied tumor enrichment effect at the time-point, subsequent *in vivo* thermal generation efficiency from the tumor located MPLa&ICG is comprehensively determined. Obviously, the tumor temperature of MPLa&ICG administrated mice increases dramatically to 52.5 °C within 2 min and finally reaches up to 60.5 °C at 6 min of continuous 808 nm laser shinning (Fig. 5E and F). Simultaneously, nonobvious thermal fluctuation in cancerous tissue is tested in PBS treated mice even after continuous NIR laser illumination for 5 min (36.6 °C), profoundly proving the gratifying capability of MPLa&ICG to suppress malignant GBM by high efficient PTT.

3.5. Synergistic tumor suppression by PTT&OXT

Above *in vitro* appreciable synergistic tumor cell killing and accurate tumor tissue distinguishing capabilities motivate us to comprehensively estimate *in vivo* tumor suppression performance. Accordingly, subcutaneous G422 tumor bearing nude mice are averagely divided into 4 groups (n = 4): PBS, PBS + L, MPLa&ICG, MPLa&ICG + L. The laser groups undergo once illumination (1.5 W/cm^2, 6 min) at 24 h of separate caudal-vein injection of PBS and MPLa&ICG. Apparently, it can be discovered that tumor volumes of PBS and PBS + L groups progressively increase during the 15 days (Fig. 6A–C, F). By contrast with other two nanoplatform treated groups, comparatively lowest overall survival rates in the range of 20%–30 % at day 60 are found in two PBS treated groups (Fig. S12), solidly verifying that only laser exposure is invalid to prevent the proliferation of cancerous cells. In agreement with the G422 cell killing outcomes, single MPLa&ICG treatment is proved to be fairly inefficacious in inhibiting tumor expansion with a slight improvement in the survival rate (Fig. 6A–C, F), further validating the imperfection of single OXT mode. Intriguingly, MPLa&ICG plus laser irradiation shows the desirable therapeutic performance with complete tumor ablation (Fig. 6A–C,F). And the survival rate overwhelming extends up to 90 % over a period of 2 months (Fig. S12), substantially implying the potent synergistic capability of PTT enhanced OXT for suppressing malignancies. The photographs of resected tumors obtained from representative mouse are weighed, as depicted in Fig. 6B–D, the data is identical with the varying tendencies of tumor growth curves. In order to intuitively detect the impairment of cancerous cells after four diverse administrations, H&E and TUNEL stained studies of tumor slices are finally performed. As presented in Fig. 6G, MPLa&ICG + L treated group presents the most serious deterioration and the largest area of necrosis. For comparison, undistinguishable damage G422 cells are observed in two PBS administrated groups. All *in vivo* antitumor outcomes maintain good consistency with the data of tumor cell killing *in vitro*, suggesting that our synergistic mode energetically evolves in inducing the highest antitumor efficacy. Significantly, no remarked body weight loss nor obvious organ pathological abnormalities (Fig. 6E–S13) is visualized in all tested groups. In a word, mesoporous La-based nanoplafrom fundamentally possesses high biosafety when utilizes in combating clinical GBM.

4. Conclusion

In summary, a lanthanum based theranostic nanoplatform with dendritic mesopores have successfully designed and formulated using a viscosity mediating self-assembly method. Benefiting from the unique morphology, the lanthanum nanosphere with dendritic meso-channels owns exceptionally high specific surface area with relatively higher amount of lanthanum active sites for extraordinarily producing ROS in tumor cells. After encapsulating of ICG in mesoporous channels, the constructed nanocomposites feature of specific tumor microenvironmental sensitivity for biodegradation, facilitating the subsequent ROS generation. Take advantages of accurate recognition of GBM cells and weak acid responsiveness, intracellular ROS is explosively amplified *via* local heat generation upon 808 nm light shining. Predominant *in vitro* and *in vivo* GBM cell killing efficiency is realized *via* OXT in conjunction with the assistance of PTT under 808 nm light exposure. Our study prompts a fascinating strategy for effectively preventing GBM growth by synergistic OXT and PTT.

CRediT authorship contribution statement

Guangwei Zheng: Writing – original draft, Software, Investigation, Formal analysis, Data curation. **Shizhong Wu:** Writing – original draft, Visualization, Supervision, Project administration, Formal analysis. **Xianming Deng:** Writing – original draft, Validation, Software, Project administration, Data curation. **Ao Wang:** Methodology, Investigation. **Yunfei Ying:** Software, Methodology, Formal analysis. **Siyaqi Li:** Methodology, Data curation. **Feifei Wang:** Validation, Investigation. **Xiaolong Liu:** Supervision, Project administration. **Peiyuan Wang:** Writing – review & editing, Validation, Project administration, Funding acquisition, Data curation, Conceptualization. **De Wei:** Writing – review & editing, Validation, Project administration, Conceptualization.

Declaration of competing interest

The authors declare that they have no known competing financial interests or personal relationships that could have appeared to influence the work reported in this paper.

Data availability

Data will be made available on request.

Acknowledgments

Appendix A. Supplementary data

Supplementary data to this article can be found online at https://doi.org/10.1016/j.mtbio.2024.101223.

References

[1] T.R. Berger, P.Y. Wen, M. Lang-Orsini, U.N. Chukwueke, World health organization 2021 classification of central nervous system tumors and implications for therapy for adult-type gliomas: a review, JAMA Oncol. 8 (2022) 1493–1501, https://doi.org/10.1001/jamaoncol.

[2] W. Wang, Y. Zhao, L. Teng, J. Yan, Y. Guo, Y. Qiu, Y. Ji, B. Yu, D. Pei, W. Duan, M. Wang, L. Wang, J. Duan, Q. Sun, S. Wang, H. Duan, C. Sun, Y. Guo, L. Luo, Z. Guo, F. Guan, Z. Wang, A. Xing, Z. Liu, H. Zhang, L. Cui, L. Zhang, G. Jiang, D. Yan, X. Liu, H. Zheng, D. Liang, W. Li, Z. Li, Z. Zhang, Neuropathologist-level integrated classification of adult-type diffuse gliomas using deep learning from whole-slide pathological images, Nat. Commun. 14 (2023) 6359, https://doi.org/10.1038/s41467-023-41195-9.

[3] H. Chen, L. Liu, A. Ma, T. Yin, Z. Chen, R. Liang, Y. Qiu, M. Zheng, L. Cai, Noninvasively immunogenic sonodynamic therapy with manganese protoporphyrin liposomes against triple-negative breast cancer, Biomaterials 26 (2021) 120639, https://doi.org/10.1016/j.biomaterials.2020.120639.

[4] Y. Huang, S. Mo, Y. Jin, Z. Zheng, H. Wang, S. Wu, Z. Ren, J. Wu, Ammonia induced excess ROS causes impairment and apoptosis in porcine IPEC-J2 intestinal epithelial cells, Ecotox. Environ. Safe. 243 (2022) 114006, https://doi.org/10.1016/j.ecoenv.2022.114006.

[5] Q. Zhang, Q. Luo, Z. Liu, M. Sun, X. Dong, Nano-ROS-generating approaches to cancer dynamic therapy: lessons from nanoparticles, Chem. Eng. J. 457 (2023) 1471225, https://doi.org/10.1016/j.cej.2022.141225.

[6] C. Glorieux, S. Liu, D. Trachootham, P. Huang, Targeting ROS in cancer: rationale and strategies, Nat. Rev. Drug Discov. 13 (2024) 1035, https://doi.org/10.1038/s41573-024-00979-4.

[7] K. Wei, Y. Wu, X. Zheng, L. Ouyang, G. Ma, C. Ji, M. Yin, A light-triggered J-aggregation-regulated therapy conversion: from photodynamic/photothermal therapy to long-lasting chemodynamic therapy for effective tumor ablation, Angew. Chem. Int. Ed. 63 (2024) e20240439, https://doi.org/10.1002/anie.202404395.

[8] Q. Zhang, J. Wu, J. Wang, X. Wang, C. Wu, M. Chen, Q. Wu, M.S. Lesniak, Y. Mi, Y. Cheng, Q. Wang, Enzyme-triggered disassembly of perylene monoimide-based nanoclusters for activatable and deep photodynamic therapy, Angew. Chem. Int. Ed. 59 (2020) 3732–3738, https://doi.org/10.1002/anie.202001107.

[9] Y. Zhao, S. Wang, Y. Ding, Z. Zhang, T. Huang, Y. Zhang, X. Wan, Z.L. Wang, L. Li, Piezotronic effect-augmented $C_{u2.}$ $_xO$-BaTiO$_3$ sonosensitizers for multifunctional cancer dynamic therapy, ACS Nano 16 (2022) 9304–9316, https://doi.org/10.1021/acsnano.2c01968.

[10] G. Yang, J.S. Ni, Y. Li, M. Zha, Y. Tu, K. Li, Acceptor engineering for optimized ROS generation facilitates reprogramming macrophages to M1 phenotype in photodynamic immunotherapy, Angew. Chem. Int. Ed. 60 (2021) 5386–5393, https://doi.org/10.1002/anie.202013228.

[11] J. An, Y. Hu, K. Cheng, C. Li, X. Hou, G. Wang, X. Zhang, B. Liu, Y. Zhao, M. Zhang, ROS-augmented and tumor-microenvironment responsive biodegradable nanoplatform for enhancing chemo-sonodynamic therapy, Biomaterials 234 (2020) 119761, https://doi.org/10.1016/j.biomaterials.2020.119761.

[12] S.B. Glass, L. Gonzalez-Fajardo, A.O.R. Beringhs, X. Lu, Redox potential and ROS-mediated nanomedicines for improving cancer therapy, Antioxid Redox Signal 30 (2019) 747–761, https://doi.org/10.1089/ars.2017.7370.

[13] Q. Wang, T. Yang, S. Li, C. Xu, C. Wang, Y. Xiong, X. Wang, J. Wan, X. Yang, Z. Li, Unimolecular self-assembled hemicyanine-oleic acid conjugate acts as a novel succinate dehydrogenase inhibitor to amplify photodynamic therapy and eliminate cancer stem cells, Research 6 (2023) 223, https://doi.org/10.34133/research.0223.

[14] A.E. Zetrini, H. Lip, A.Z. Abbasi, I. Alradwan, T. Ahmed, C. He, J.T. Henderson, A.M. Rauth, X.Y. Wu, Remodeling tumorimmune microenvironment by using polymer-lipid-manganese dioxide nanoparticles with radiation therapy to boost immune response of castration-resistant prostate cancer, Research 6 (2023) 247, https://doi.org/10.34133/research.0247.

[15] C. Zhang, D. Xia, J. Liu, D. Huo, X. Jiang, Y. Hu, Bypassing the immunosuppression of myeloid-derived suppressor cells by reversing tumor hypoxia using a platelet-inspired platform, Adv. Funct. Mater. 30 (2020) 2000189, https://doi.org/10.1002/adfm.202000189.

[16] H. Huang, C. Zhang, X. Wang, J. Shao, C. Chen, H. Li, C. Ju, J. He, H. Gu, D. Xia, Overcoming hypoxia-restrained radiotherapy using an erythrocyte-inspired and glucose-activatable platform, Nano Lett. 20 (2020) 4211–4219, https://doi.org/10.1021/acs.nanolett.0c00650.

[17] F. Gao, Y. Tang, W.L. Liu, M.Z. Zou, C. Huang, C.J. Liu, X.Z. Zhang, Intra/extracellular lactic acid exhaustion for synergistic metabolic therapy and immunotherapy of tumors, Adv. Mater. 31 (51) (2019) e1904639, https://doi.org/10.1002/adma.201904639.

[18] G. Yang, L. Xu, Y. Chao, J. Xu, X. Sun, Y. Wu, R. Peng, Z. Liu, Hollow MnO_2 as a tumor-microenvironment-responsive biodegradable nano-platform for combination therapy favoring antitumor immune responses, Nat. Commun. 8 (1) (2017) 902, https://doi.org/10.1038/s41467-017-01050-0.

[19] X. Wei, Y. Chen, X. Jiang, M. Peng, Y. Liu, Y. Mo, D. Ren, Y. Hua, B. Yu, Y. Zhou, Q. Liao, H. Wang, B. Xiang, M. Zhou, X. Li, G. Li, Y. Li, W. Xiong, Z. Zeng, Mechanisms of vasculogenic mimicry in hypoxic Tumor microenvironments, Mol. Cancer 20 (2021) 7, https://doi.org/10.1186/s12943-020-01288-1.

[20] Q. Wu, L. You, E. Nepovimova, Z. Heger, W. Wu, K. Kuca, V. Adam, Hypoxia-inducible factors: master regulators of hypoxic Tumor immune Escape, J. Hematol. Oncol. 15 (2022) 77, https://doi.org/10.1186/s13045-022-01292-6.

[21] T. He, C. Jiang, J. He, Y. Zhang, G. He, J. Wu, L. Jing, X. Zhou, P. Huang, Manganese-dioxide-coating-instructed plasmonic modulation of gold nanorods for activatable duplex-imaging-guided NIR-II photothermal-chemodynamic therapy, Adv. Mater. 33 (13) (2021) e2008540, https://doi.org/10.1002/adma.202008540.

[22] B. Ding, P. Zheng, P. Ma, J. Lin, Manganese oxide nanomaterials: synthesis, properties, and theranostic applications, Adv. Mater. 32 (10) (2020) e1905823. https://doi:10.1002/adma.202008540.

[23] H. Ji, H. Hu, Q. Tang, X. Kang, X. Liu, L. Zhao, R. Jing, M. Wu, G. Li, X. Zhou, J. Liu, Q. Wang, H. Cong, L. Wu, Y. Qin, Precisely controlled and deeply penetrated micro-nano hybrid multifunctional motors with enhanced antibacterial activity against refractory biofilm infections, J. Hazard Mater. 436 (2022) 129210, https://doi.org/10.1016/j.jhazmat.2022.129210.

[24] C. Jia, Y. Guo, F.G. Wu, Chemodynamic therapy via Fenton and Fenton-Like nanomaterials: strategies and recent advances, Small 18 (2021) e2103868, https://doi.org/10.1002/smll.202103868.

[25] X. Liu, Z. Yan, Y. Zhang, Z. Liu, Y. Sun, J. Ren, X. Qu, Two-dimensional metal-organic framework/enzyme hybrid nanocatalyst as a benign and self-activated cascade reagent for in vivo wound healing, ACS Nano 13 (2019) 5222–5230, https://doi.org/10.1021/acsnano.8b09501.

[26] Y. Nosaka, A.Y. Nosaka, Generation and detection of reactive oxygen species in photocatalysis, Chem. Rev. 117 (17) (2017) 11302–11336, https://doi.org/10.1021/acs.chemrev.7b00161.

[27] Y. Xiang, Q. Chen, Y. Nan, M. Liu, Z. Xiao, Y. Yang, J. Zhang, X. Ying, X. Long, S. Wang, J. Sun, Q. Huang, K. Ai, Nitric oxide-based nanomedicines for conquering TME fortress: say "NO" to insufficient tumor treatment, Adv. Funct. Mater. 34 (13) (2024) 2312092, https://doi.org/10.1002/adfm.202312092.

[28] C. Zuo, J. Xia, L. Chen, Nitric oxide-based nanomedicines for conquering TME fortress: say "NO" to insufficient tumor treatment, Nat. Commun. 15 (2023) 5057, https://doi.org/10.1002/adfm.202312092.

[29] D. Maggiorani, O. Le, V. Lisi, S. Landais, G. Moquin-Beaudry, V.P. Lavallée, H. Decaluwe, C. Beauséjour, Senescence drives immunotherapy resistance by inducing an immunosuppressive tumor microenvironment, Nat. Commun. 15 (2024) 2435, https://doi.org/10.1038/s41467-024-46769-9.

[30] K. Inagaki, H. Haraguchi, Determination of rare earth elements in human blood serum by inductively coupled plasma mass spectrometry after chelating resin preconcentration, Analyst 125 (2020) 191–196, https://doi.org/10.1039/a907781b.

[31] E.E. Lachine, A.A. Noujaim, C. Ediss, L.I. Wiebe, Toxicity, tissue distribution and excretion of 46ScCl3 and 46Sc-EDTA in mice, Int. J. Appl. Radiat. Isot. 27 (1976) 373–377, https://doi.org/10.1016/0020-708X(76)90091-0.

[32] V.M. Lu, K.L. McDonald, H.E. Townley, Realizing the therapeutic potential of rare earth elements in designing nanoparticles to target and treat glioblastoma, Nanomedicine (Lond) 12 (2017) 2389–2401, https://doi.org/10.2217/nnm-2017-0193.

[33] A.L. Bulin, M. Broekgaarden, F. Chaput, V. Baisamy, J. Garrevoet, B. Busser, D. Brueckner, A. Youssef, J.L. Ravanat, C. Dujardin, V. Motto-Ros, F. Lerouge, S. Bohic, L. Sancey, H. Elleaume, Radiation dose-enhancement is a potent radiotherapeutic effect of rare-earth composite nanoscintillators in preclinical models of glioblastoma, Adv. Sci. 200 (2020) 1675, https://doi.org/10.1002/advs.202001675.

[34] G. Zhuang, Y. Zhou, H. Lu, W. Lu, M. Zhou, Y. Wang, M. Tan, Concentration of rare earth elements As, and Th in human brain and brain tumors, determined by neutron activation analysis, Biol. Trace Elem. Res. 53 (1996) 45–49, https://doi.org/10.1007/BF02784543.

[35] V.M. Lu, R.T. Jue, K.L. McDonald, Cytotoxic lanthanum oxide nanoparticles sensitize glioblastoma cells to radiation therapy and temozolomide: an in vitro rationale for translational studies, Sci. Rep. 10 (2020) 18156, https://doi.org/10.1038/s41598-020-75372-3.

[36] J. Wu, J. Yang, Q. Liu, S. Wu, H. Ma, Y. Cai, Lanthanum induced primary neuronal apoptosis through mitochondrial dysfunction modulated by Ca^{2+} and bcl-2 family, Biol. Trace Elem. Res. 152 (2013) 125–134, https://doi.org/10.1007/s12011-013-9601-3.

[37] L. Shen, Z. Lan, X. Sun, L. Shi, Z. Lan, X. Sun, L. Shi, Q. Liu, J. Ni, Proteomic analysis of lanthanum citrate-induced apoptosis in human cervical carcinoma SiHa cells, Biomaterials 23 (2010) 1179–1189, https://doi.org/10.1007/s10534-010-9368-3.

[38] F. Feyerabend, J. Fischer, J. Holtz, F. Witte, R. Willumeit, H. Drücker, C. Vogt, N. Hort, Evaluation of short-term effects of rare earth and other elements used in magnesium alloys on primary cells and cell lines, Acta Bio 6 (2010) 1834–1842.

[39] J. Karges, Encapsulation of Ru(II) polypyridine complexes for tumor-targeted anticancer therapy, BME Front 4 (2023) 24, https://doi.org/10.34133/bmef.0024.

[40] R. Wang, R.J. Deutsch, E.D. Sunassee, B.T. Crouch, N. Ramanujam, Adaptive design of fluorescence imaging systems for custom resolution, fields of view, and geometries, BME Front. 4 (2023) 5, https://doi.org/10.34133/bmef.0005.

[41] L. Xu, Z. Li, Y. Ma, L. Lei, R. Yue, H. Cao, S. Huan, W. Sun, G. Song, Imaging Carotid Plaque Burden in Living Mice via Hybrid Semiconducting Polymer Nanoparticles-Based Near-Infrared-II Fluorescence and Magnetic Resonance Imaging, Research, vol. 6, 2023, p. 186, https://doi.org/10.34133/research.0186.

[42] Q. Chen, Q. Zhong, Z. Liu, P. Li, T. Lin, Q. Zheng, J. Wang, J. Lin, J. Lu, L. Cao, M. Lin, R. Tu, Z. Huang, G. Zeng, M. Jiang, H. Wang, X. Huang, K. Xu, Y. Li, C. Zheng, J. Xie, C. Huang, Indocyanine green fluorescence imaging-guided versus conventional laparoscopic lymphadenectomy for gastric cancer: long-term outcomes of a phase 3 randomised clinical trial, Nat. Commun. 4 (2023) 147413, https://doi.org/10.1038/s41467-023-42712-6.

[43] T. Hsu, Y. Chen, R. Zhang, Z. Chen, C. Wu, W. Chang, C. Mou, H.W. Chan, S. Wu, Overcoming the blood–brain tumor barrier with docetaxel-loaded mesoporous silica nanoparticles for treatment of temozolomide-resistant glioblastoma, ACS Nano 16 (17) (2024) 21722–21735, https://doi.org/10.1021/acsami.4c04289.

[44] Y. Feng, Z. Liao, M. Li, H. Zhang, T. Li, X. Qin, S. Li, C. Wu, F. You, X. Liao, L. Cai, H. Yang, Y. Liu, Mesoporous silica nanoparticles-based nanoplatforms:basic construction, current state, and EmergingApplications in anticancer therapeutics, Adv. Healthcare Mater. 12 (2023) 2201884, https://doi.org/10.1002/adhm.202201884.

[45] S. Wu, R. Han, Y. Yan, W. Chen, W. Gao, Y. Hou, K. Tang, Porous CeO_2 nanorods loaded with indocyanine green for enhanced tumor-specific therapy, Micropor. Mesopor. Mat. 315 (2021) 110905, https://doi.org/10.1016/j.micromeso.2021.110905.

[46] R. Yang, P. Wang, K. Lou, Y. Dang, H. Tian, Y. Li, Y. Gao, W. Huang, Y. Zhang, X. Liu, G. Zhang, Biodegradable nanoprobe for NIR-II fluorescence image-guided surgery and enhanced breast cancer radiotherapy efficacy, Adv. Sci. 9 (2022) e2104728. https://doi,10.1002/advs.202104728.